Fully kinetic simulations of strong steady-state collisional planar plasma shocks

S. E. Anderson,[*] L. Chacón, W. T. Taitano, A. N. Simakov, and B. D. Keenan

Los Alamos National Laboratory, Los Alamos, New Mexico 87545, USA

We report on simulations of strong, steady-state collisional planar plasma shocks with fully kinetic ions *and* electrons, independently confirmed by two fully kinetic codes (an Eulerian continuum and a Lagrangian particle-in-cell). While kinetic electrons do not fundamentally change the shock structure as compared with fluid electrons, we find an appreciable rearrangement of the preheat layer, associated with nonlocal electron heat transport effects. The electron heat-flux profile qualitatively agrees between kinetic- and fluid-electron models, suggesting a certain level of "stiffness," though substantial nonlocality is observed in the kinetic heat flux. We also find good agreement with nonlocal electron heat-flux closures proposed in the literature. Finally, in contrast to the classical hydrodynamic picture, we find a significant collapse in the "precursor" electric-field shock at the preheat layer leading edge, which correlates with the electron-temperature gradient relaxation.

I. INTRODUCTION

.Strong shocks are present in a variety of high-energy-density (HED) environments, including inertial confinement fusion (ICF) capsule implosions [1–3]. Given the role of shocks in ICF compression and yield, it is important to understand the impact that kinetic effects may have in the shock structure, and its imprint on the imploding capsule (e.g., Ref. [4]). This is relevant, as the state-of-the-art for simulating ICF capsule implosions is radiation hydrodynamics (rad-hydro), which is only strictly valid in systems with small Knudsen numbers (defined later)—which are highly collisional—and therefore only accurate for weak shocks with $M \sim 1$ [5]. The impact of kinetic ions on shock structure relative to rad-hydro simulations has been studied by Keenan *et al.* [6,7], and manifests itself in significant changes of the ion species concentration and temperature separation. The presence of kinetic electrons may impact HED plasma systems by potentially changing the shock structure through nonlocal heat transport (which may affect ion shock dynamics [7]), or, in the case of ICF implosions, introducing hot-electron preheat (which may, e.g., alter the implosion adiabat). Here, we focus on the former.

Rad-hydro has been used extensively to investigate strong plasma shocks [8–13]. The classical structure of a strong collisional plasma shock exhibits, from upstream to downstream (see, e.g., Ref. [13]) (1) a prominent preheat layer wherein the electron temperature T_e exceeds that of the ions T_i, (2) an embedded ion compression shock, where the density jump occurs and T_i increases rapidly and surpasses that of the electrons, and (3) a region of ion-electron temperature equilibration. The preheat and relaxation regions [(1) and (3)] are approximately of width $\approx Z_i^2 (m_i/m_e)^{1/2} \lambda_{ii}^{DS}$ (where m_i, m_e, Z_i, and λ_{ii}^{DS} are the ion and electron masses, the ion charge, and

the ion-ion downstream mean free path, respectively), while the embedded compression shock is of order several λ_{ii}^{DS}.

To date, kinetic studies of strong plasma shocks have focused on ions, and have thus been performed almost exclusively with "hybrid" kinetic codes employing a fluid-electron model coupled with a kinetic-ion Vlasov-Fokker-Planck (VFP) description [6,7,14–16]. In these codes, the fluid electrons are quasineutral and ambipolar, with T_e determined from the electron energy equation and with the electron heat flux modeled as the Braginskii/Spitzer-Härm expression (i.e., $\mathcal{Q}_{\mathrm{Brag.},e} = -\kappa_e \nabla T_e$, $\kappa_e \propto T_e^{5/2}$ [17]), usually with some variety of heat-flux limiter, $|\mathcal{Q}_e| = \min(f_{\lim} \mathcal{Q}_{\mathrm{FS},e}, |\mathcal{Q}_{\mathrm{Brag.},e}|)$, where $f_{\lim}$ is effectively a "tuning knob" to prevent faster-than-streaming diffusion, and $\mathcal{Q}_{\mathrm{FS},e} = n_e T_e v_{\mathrm{th},e}$ is the free-streaming thermal flux. However, it is known that local fluid models of the electron heat flux are only valid for sufficiently small electron Knudsen numbers (defined as the particle mean free path λ over a characteristic gradient length scale L_∇, $\mathrm{Kn} = \lambda/L_\nabla$), $\mathrm{Kn}_e \lesssim 10^{-3}$. For $\mathrm{Kn}_e \gtrsim 10^{-3}$, we expect to begin observing deviations from the fluid results (see Refs. [18,19]).

We note that sophisticated models for nonlocal electron heat flux have been proposed [e.g., the Luciani-Mora-Virmont (LMV) model [20–23]]. Several of these models were investigated in Ref. [24] with strong planar plasma shocks, using the kinetic ion code FPION [14–16], and were compared with a kinetic-electron code in Ref. [25]. However, the kinetic-electron solver was not self-consistently coupled to the kinetic ions. This approach also utilized a low-order expansion in spherical harmonics and neglected anisotropy in the collision operators, which limited the degree to which effects of non-Maxwellian distributions (including nonlocal transport) could be captured [26]. Thus, a comparison of these nonlocal electron heat-flux models with fully kinetic self-consistent simulations is still needed.

Recently, Zhang *et al.* published results of fully kinetic particle-in-cell simulations for an $M \approx 3$ piston-driven

*andeste@lanl.gov

planar plasma shock [27]. Unfortunately, the approach possesses some significant limitations. First, their simulations were terminated before the shock detached from the piston; second, the total simulation time was less than the ion-electron thermal equilibration time [28]; third, the simulation domain was of order the shock width. Thus, their solution is transient and not yet relaxed to steady state. This is confirmed by the fact that T_e is nonmonotonic and concave upward in the preheat layer [see their Fig. 4(b)], in a significant contrast to what is expected for a steady-state planar shock (see, e.g., Ref. [10]).

In this article, we present self-consistent simulations of strong *steady-state* collisional planar plasma shocks. We performed these simulations with two different fully kinetic codes (an Eulerian continuum and a Lagrangian particle-in-cell) with the goal of cross-code verification, and found excellent agreement. The simulations employed a realistic electron-ion mass ratio. We find that, while kinetic electrons do not fundamentally change the structure of the shock as compared with fluid electrons, they do modify appreciably the preheat layer structure. In particular, the sharp electron-temperature gradient at the front of the preheat layer disappears, and average ion-electron temperature separation there decreases by about 20%. The rearrangement of the electron-temperature profile in the preheat layer can be traced to nonlocal electron heat transport effects due to the kinetic behavior of electrons. Moreover, we find that the electron heat-flux profile displays "stiffness" in that it qualitatively agrees remarkably well between fluid- and kinetic-electron models, demanding adjustments in the corresponding electron-temperature profile. We also verify the LMV nonlocal electron heat-flux closures proposed in the literature against self-consistent full VFP simulations, and find them to provide a reasonable agreement with the high-fidelity simulations.

II. PROBLEM SETUP

To study this problem, we employ the Eulerian VFP code iFP [29–32], and the Lagrangian code VPIC [33–35]. The iFP code solves the coupled VFP equations for each of the plasma species in a one-dimensional (1D) planar electrostatic approximation, with the electric field given by the 1D Ampère equation

$$\partial_t f_\alpha + \partial_x(v_\parallel f_\alpha) + \frac{Z_\alpha e}{m_\alpha} E_\parallel \partial_{v_\parallel} f_\alpha = \sum_{\beta=1}^{N_s} C_{\alpha\beta}, \quad (1)$$

$$\epsilon_0 \partial_t E_\parallel + \sum_{\alpha=1}^{N_s} Z_\alpha e n u_{\parallel,\alpha} = 0, \quad (2)$$

where α, β denote the species index, f_α is the particle distribution function for species α, the symbols Z_α and m_α indicate the species α particle charge and mass, and e is the proton charge. The electric field and α-species bulk velocity in the shock propagation direction are denoted by $E_\parallel$ and $u_{\parallel,\alpha}$, respectively. We denote vector components along the spatial direction of the shock propagation (x) with the subscript $\parallel$, while perpendicular components are denoted with the subscript $\perp$. We note that, in the 1D electrostatic approximation, we may without

loss of generality consider a cylindrically symmetric velocity space ($v_\parallel$, $v_\perp$). The VPIC code is a fully 3D electromagnetic particle-in-cell code. However, for the simulations presented here, the computational domain is 1D in configuration space, and no electromagnetic phenomena are observed to develop. We note that in a "real" (i.e., 3D and electromagnetic) system, there may be a variety of rich behavior, including instabilities such as the Richtmyer-Meshkov (hydrodynamic) [36] or Weibel (kinetic) [37]. However, 3D and electromagnetic effects will be *driven by* and appear as a *modification of* the underlying 1D structure, which it is vital to understand.

We consider an $M = 6$ planar collisional shock in a protium plasma with the realistic mass ratio $m_p/m_e = 1836$. The computations are performed in the frame of the shock, and are initialized with the Rankine-Hugoniot (RH) relations as upstream and downstream (Maxwellian) boundary conditions, with a hyperbolic tangent transition in between. Note that as the simulation is performed in the frame of the shock, and run to a steady state, the details of the hyperbolic transition in the initial condition do not affect the final (steady-state) solution. The initial distribution functions are Maxwellian. To allow room for the downstream equilibration zone, the shock position is located at $x/L = 0.4$, with L the total domain length. Unless otherwise specified, the simulation domain spans 250 downstream ion-ion mean free paths, i.e., $L = 250\lambda_{ii}^{\mathrm{DS}}$. In the regime considered here, the Debye length λ_D is much smaller than collisional mean free paths, $\lambda_D \ll \lambda_{ii}$.

The VPIC simulations were initialized by sampling from steady-state iFP ion and electron distribution functions over a truncated spatial domain ($L = 130\lambda_{ii}^{\mathrm{DS}}$) and run to steady state. The boundaries are Maxwellian, based on the RH relations. To mitigate the noise inherent in the particle-in-cell simulations, we have applied a Savitzky-Golay filter [38] (polynomial order $p = 3$, filter window width $\sim 2\lambda_{ii}^{\mathrm{DS}}$) to smooth the VPIC moment profiles. The spatial profiles presented here are truncated to a span of $130\lambda_{ii}^{\mathrm{DS}}$ to match the VPIC simulation domain. In the following results, all quantities are normalized with respect to the downstream values. Normalization constants may be found in the Appendix.

"Bulk" plasma quantities (such as the temperature, velocity, etc.) are defined for kinetic species from appropriate velocity-space moments of the kinetic distribution functions. For a species α, the number density n_α, bulk velocity $\boldsymbol{u}_\alpha$, and total energy density ε_α are defined from the distribution function f_α by

$$n_\alpha = \int_{\boldsymbol{v}} f_\alpha d\boldsymbol{v}, \quad (3)$$

$$n_\alpha \boldsymbol{u}_\alpha = \int_{\boldsymbol{v}} \boldsymbol{v} f_\alpha d\boldsymbol{v}, \quad (4)$$

$$\varepsilon_\alpha = \frac{3}{2} n_\alpha T_\alpha + \frac{1}{2} m_\alpha n_\alpha \boldsymbol{u}_\alpha^2 = \int_{\boldsymbol{v}} \frac{1}{2} m_\alpha \boldsymbol{v}^2 f_\alpha d\boldsymbol{v}. \quad (5)$$

The temperature T_α is then obtained by rearranging Eq. (5), utilizing Eqs. (3) and (4).

III. RESULTS

In Fig. 1 (left and center), we see the spatial profiles of temperature and temperature difference ($T_e - T_i$) for ions and
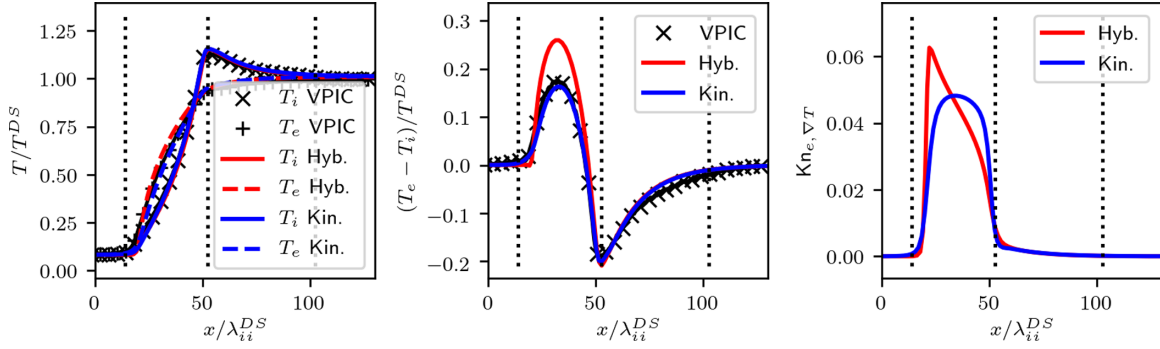
FIG. 1. Left: Spatial profiles of T_i and T_e normalized to the downstream limit for hybrid iFP (fluid electrons and kinetic ions, Hyb., red lines), fully kinetic iFP (Kin., blue lines), and VPIC (symbols). Center: Spatial profiles of the temperature difference $T_e - T_i$ clearly showing a kinetic suppression of the temperature separation in the preheat layer. Right: Spatial profiles of $\mathrm{Kn}_{e,\nabla T}$ for hybrid (Hyb.) and fully kinetic (Kin.) iFP simulations. Vertical dotted lines indicate (from left to right) the approximate locations of the upstream edge of the preheat layer, the compression shock, and the downstream edge of the relaxation layer.

electrons in the shock comparing hybrid (kinetic ions and fluid electrons) to fully kinetic simulations. Profiles of the bulk velocity and density moments do not change appreciably between hybrid and fully kinetic simulations. Here, the main difference between hybrid and fully kinetic results is the suppression of the $\delta T = T_e - T_i$ in the preheat layer ($x \sim 15$–55) by approximately 20%, with T_e relaxing towards T_i (see Fig. 1 center). The temperature profiles through the compression shock and into the downstream equilibration layer are essentially unchanged between the fluid- and kinetic-electron treatments.

In Fig. 1 (right), we compare the electron Knudsen number based upon the temperature-gradient length scale [$\mathrm{Kn}_{e,\nabla T} \equiv \lambda_e |\nabla(\ln T_e)|$] for fully kinetic and hybrid iFP simulations. We use the temperature-gradient length scale in particular because of its relevance in fluid-electron transport models (see, e.g., Refs. [18,19]). We see that $\mathrm{Kn}_{e,\nabla T}$ is approximately 5×10^{-2} throughout the preheat layer (well above the $\mathrm{Kn}_e \sim 10^{-3}$ threshold), which corresponds exactly to where the electron-temperature profile has been adjusted in Fig. 1, and is much smaller elsewhere. Notably, the sharp peak in the fluid-electron $\mathrm{Kn}_{e,\nabla T}$ profile at the preheat layer upstream edge (where $\partial_x T_e$ is largest) is smoothed significantly in the kinetic-electron case. In all the results that follow, unless otherwise specified, the "kinetic" results are from the iFP (Eulerian VFP) code.

To look deeper into differences between hybrid and fully kinetic simulations, we examine the terms in the electron energy equation [see Eq. (A3) of Ref. [39]]. Upon rearranging, we find the energy equation may be expressed as

$$\frac{\partial_x \mathscr{Q}_{\|,e}}{T_e} \approx n_e u_{\|,e} \left[\partial_x(\ln n_e) - \frac{3}{2} \partial_x(\ln T_e) \right]. \quad (6)$$

Here, we neglect the temporal derivatives, as we are in the frame of the shock and the simulations are allowed to reach a steady state. Further, we utilize the facts that (1) with $u_{\|,e} = u_{\|,i}$, frictional energy exchange may be neglected and (2) the momentum $n_e u_{\|,e}$ is constant. The viscous stress and thermal relaxation terms may be neglected essentially by assuming that the electron-ion mass ratio is smaller than the electron Knudsen number, $\frac{m_e}{m_i} \ll \mathrm{Kn}_{e,\nabla}$, and that $\delta\hat{T}_e < 1$, where $\delta\hat{T}_e \equiv |T_i - T_e|/T_e$. As the particle flux density $n_e u_{\|,e}$ is constant

through the shock, Eq. (6) clearly expresses that the ratio of the divergence of the electron heat flux to the electron temperature is dependent only on the two inverse length scales, $L_{T_e}^{-1} \equiv |\partial_x(\ln T_e)|$ and $L_{n_e}^{-1} \equiv |\partial_x(\ln n_e)|$. This is demonstrated in Fig. 2, which shows the left-hand side of Eq. (6) (top) and the inverse gradient length scales for the electron-temperature and electron-density profiles (bottom). From this, we can clearly conclude that the primary effect of the kinetic electrons is to smooth the steep electron-temperature gradient at the leading preheat layer edge where the Knudsen number (based on T_e) is the largest.
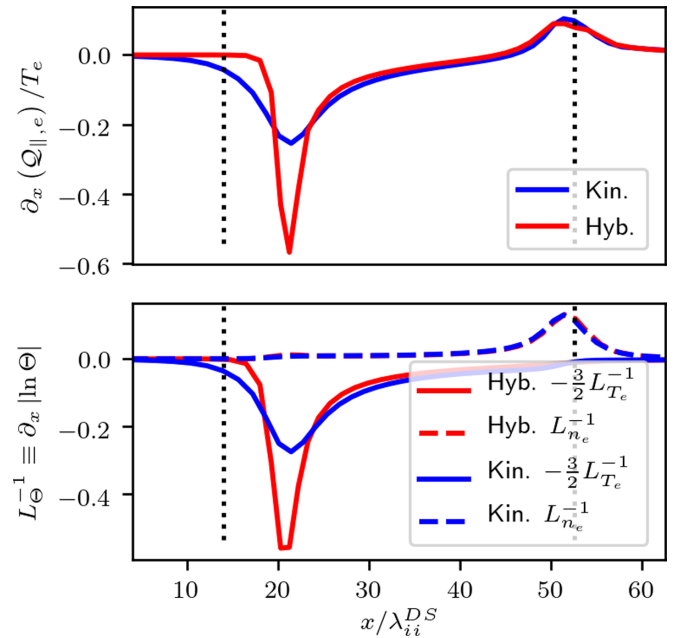

FIG. 2. Top: Spatial profiles within the preheat region for the $\partial_x \mathscr{Q}_{\|,e}/T_e$ term in Eq. (6) for hybrid (Hyb.) and fully kinetic (Kin.) simulations. Bottom: Spatial profiles of the inverse gradient length scales based on T_e (solid) and n_e (dashed) for hybrid (Hyb.) and fully kinetic (Kin.) simulations. Vertical dotted lines indicate (from left to right) the approximate locations of the upstream edge of the preheat layer and the compression shock.
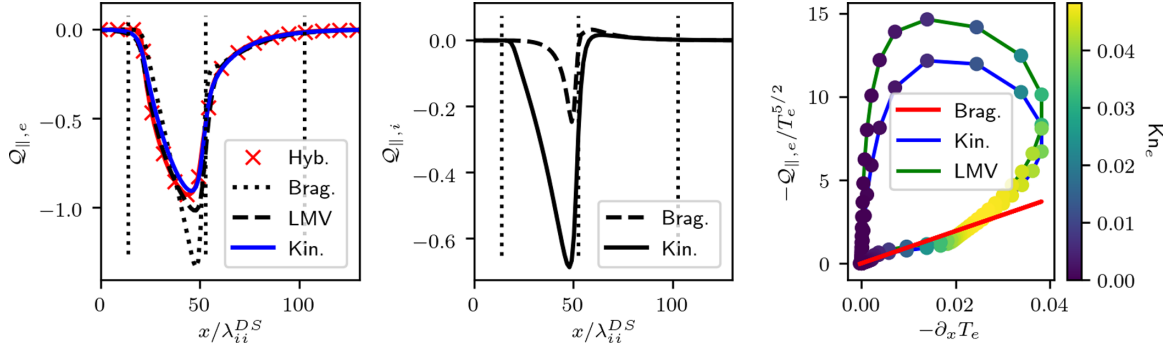
FIG. 3. Left: Spatial profiles of the electron heat fluxes $\mathcal{Q}_{\parallel,e}^{\text{Hyb.}}$ (Hyb.), $\mathcal{Q}_{\parallel,e}^{\text{Kin.}}$ (Kin.), $\mathcal{Q}_{\parallel,e,\text{Brag}}^{\text{Kin.}}$ (Brag.), and $\mathcal{Q}_{\parallel,e,\text{LMV}}^{\text{Kin.}}$ (LMV). The latter two heat fluxes employ the fully kinetic-electron moments. Note the similarity of $\mathcal{Q}_{\parallel,e}^{\text{Hyb.}}$ and $\mathcal{Q}_{\parallel,e}^{\text{Kin.}}$. Center: Spatial profiles of the ion heat fluxes $\mathcal{Q}_{\parallel,i}^{\text{Kin.}}$ (Kin.) and $\mathcal{Q}_{\parallel,i,\text{Brag}}^{\text{Kin.}}$ (Brag.). Note $\mathcal{Q}_{\parallel,i}^{\text{Kin.}}$ is comparable in magnitude to $\mathcal{Q}_{\parallel,e}^{\text{Kin.}}$. Right: Phase-space plot of the electron heat flux comparing $\mathcal{Q}_{\parallel,e}^{\text{Kin.}}$ (Kin.), $\mathcal{Q}_{\parallel,e}^{\text{Hyb.}}$ (Brag.), and $\mathcal{Q}_{\parallel,e,\text{LMV}}^{\text{Kin.}}$ (LMV). The heat-flux curves for $\mathcal{Q}_{\parallel,e}^{\text{Kin.}}$ and $\mathcal{Q}_{\parallel,e,\text{LMV}}^{\text{Kin.}}$ have symbols colored by local Knudsen numbers.

It follows from Fig. 1 (right) and Fig. 2 that, in the preheat layer, $T_e^{\text{Kin.}} \sim T_e^{\text{Hyb.}}$ and $L_{T_e}^{\text{Kin.}} \sim 2L_{T_e}^{\text{Hyb.}}$. Then, Eq. (6) predicts in this region $\mathcal{Q}_{\parallel,e}^{\text{Kin.}} \approx \mathcal{Q}_{\parallel,e}^{\text{Hyb.}}$. Figure 3 (left) demonstrates this quite clearly by showing spatial profiles of the kinetic-electron parallel heat flux $\mathcal{Q}_{\parallel,e}^{\text{Kin.}}$ and the heat flux in the hybrid simulation $\mathcal{Q}_{\parallel,e}^{\text{Hyb.}}$ based upon the Braginskii expression. Here, we compute the kinetic heat flux for a species α from its distribution function f_α using

$$\mathcal{Q}_{\parallel,\alpha}^{\text{Kin.}} = \int_{\boldsymbol{v}} \frac{1}{2} m_\alpha (\boldsymbol{v} - \boldsymbol{u}_\alpha)^2 (v_\parallel - u_{\parallel,\alpha}) f_\alpha d\boldsymbol{v}, \qquad (7)$$

where $\boldsymbol{u}_\alpha$ is the α-species bulk velocity. For comparison, we also compute from the kinetic-electron moments the Braginskii heat flux $\mathcal{Q}_{\parallel,e,\text{Brag}}^{\text{Kin.}}$ and a heat flux from the LMV model $\mathcal{Q}_{\parallel,e,\text{LMV}}^{\text{Kin.}}$. In doing so, we aim to assess the consistency of a given model with respect to the kinetic solution. If a given heat-flux model is postprocessed from the kinetic moments and agrees well with the self-consistent kinetic heat flux, we surmise that it is a good closure. That is, we hypothesize that if it were run self-consistently with the fluid-electron model in a hybrid simulation, it would produce similar moment profiles to the kinetic ones (e.g., for the temperature). The LMV model is a nonlocal closure of the form

$$\mathcal{Q}_{\parallel,\text{LMV}} = \int_{-\infty}^{+\infty} W(x, x') \mathcal{Q}_{\parallel,\text{Brag}}(x') \frac{dx'}{a\lambda_e(x')}, \qquad (8)$$

where $W(x, x')$ is a phenomenologically chosen delocalization kernel for the Braginskii heat flux, $\lambda_e(x')$ is an appropriate delocalization length scale (related to the mean free path and containing a correction accounting for the electric potential [21,22]), and a is a heuristically chosen parameter. We refer the reader to Ref. [22] for details of the model and the parameters chosen. Physically, Eq. (8) may be understood as a convolution of the local Braginskii heat flux into the surrounding space. We note that, as we expected from the analysis of Eq. (6) and Fig. 2, the kinetic and hybrid heat fluxes $\mathcal{Q}_{\parallel,e}^{\text{Kin.}}$ and $\mathcal{Q}_{\parallel,e}^{\text{Hyb.}}$ are very similar in overall magnitude and shape. The difference in the profile is essentially in a "smoothing" of the gradients at the upstream edge of the preheat layer (the same modification as seen in the electron-temperature profile). For the postprocessed heat-flux models based on the

kinetic-electron-moment profiles, we see that the LMV heat flux $\mathcal{Q}_{\parallel,e,\text{LMV}}^{\text{Kin.}}$ does very well, while $\mathcal{Q}_{\parallel,e,\text{Brag}}^{\text{Kin.}}$ is quite different. For reference, the kinetic ion heat flux $\mathcal{Q}_{\parallel,i}^{\text{Kin.}}$ and the corresponding Braginskii heat flux $\mathcal{Q}_{\parallel,i,\text{Brag}}^{\text{Kin.}}$ are also included in Fig. 3 (center). There, we observe that $\mathcal{Q}_{\parallel,i}^{\text{Kin.}}$ is actually of the same order of magnitude as $\mathcal{Q}_{\parallel,e}^{\text{Kin.}}$ and is substantially larger than $\mathcal{Q}_{\parallel,i,\text{Brag}}^{\text{Kin.}}$, in significant contrast to the usual ordering of $|\mathcal{Q}_{\parallel,i}| \sim \sqrt{\frac{m_e}{m_i}} |\mathcal{Q}_{\parallel,e}|$ [18].

Despite the similarity between hybrid and kinetic-electron heat fluxes, a detailed analysis reveals deeper physical differences. In particular, we find clear evidence of nonlocal transport effects in the kinetic-electron simulation, as expected from weakly collisional conditions. This is evidenced in Fig. 3 (right), where we show a phase-space plot of $\mathcal{Q}_{\parallel,e}/T_e^{5/2}$ from iFP simulations versus $\partial_x T_e$, with symbols colored according to the local Knudsen number. We see that the kinetic heat flux demonstrates a significant departure from the Braginskii model, with the nonlocal kinetic heat flux possessing a distinct multivalued dependence on the temperature gradient. Notably, the LMV heat-flux model also demonstrates a very similar nonlocal behavior, though it appears to overpredict slightly the nonlocality relative to the true kinetic heat flux. We note the LMV without an electric-field correction (i.e., the original model of Luciani *et al.* [20], not shown here) overpredicts the heat flux by as much as a factor of 2 [the peak in Fig. 3 (right) would be nearer to $-\mathcal{Q}_{\parallel,e}/T_e^{5/2} = 30$], though with a similar qualitative shape. Thus, since the LMV heat-flux model is largely consistent with both the heat flux and moments from the kinetic simulations, we conclude that it is a promising nonlocal heat-flux closure (at least for similar problems). This will be tested in future work.

The electric field $E_\parallel$ shows further differences between hybrid and fully kinetic simulations. In the fully kinetic simulation, $E_\parallel$ is evaluated self-consistently from Eq. (2), while in the hybrid simulation it is obtained from the electron momentum equation by neglecting electron inertia and viscosity,

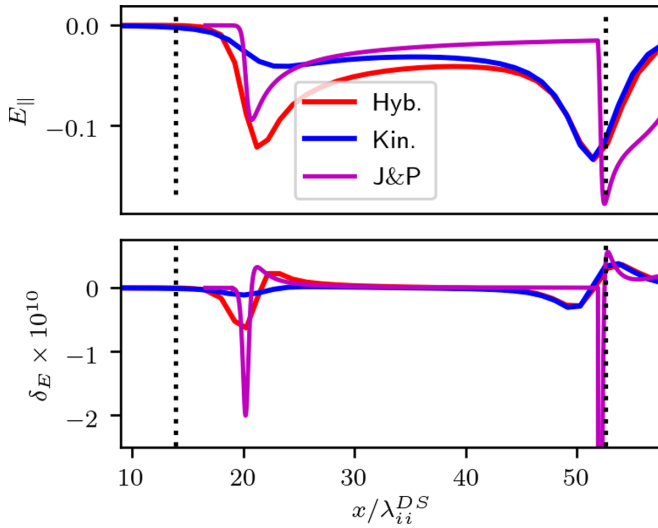$$E_\parallel = \frac{1}{q_e n_e}\left[\partial_x(n_e T_e) - \sum_i F_{\parallel,ei}\right], \qquad (9)$$

FIG. 4. Top: Spatial profiles of $E_\parallel$ from hybrid (Hyb.) and fully kinetic iFP (Kin.) simulations. Also included is the estimated electric field from the semianalytic solution of Ref. [10] (J&P). Bottom: Spatial profiles of the charge separation quantity δ_E, again comparing hybrid and fully kinetic iFP and the semianalytic estimate of Ref. [10]. Vertical dotted lines indicate (from left to right) the approximate locations of the upstream edge of the preheat layer and the compression shock.

where $F_{\parallel,ei}$ is the electron-ion friction force (for details, see Appendix A of Ref. [39]). Note that in this problem the bulk velocity of both species is identical, so $F_{\parallel,ei} \propto -\partial_x T_e$. In Fig. 4 (top), we see the spatial profiles of $E_\parallel$ for hybrid and fully kinetic iFP simulations. As expected, the most noticeable difference is in the preheat layer, where the Knudsen number is large and thus the electron-temperature gradient in the fully kinetic case has been significantly reduced, and the fully kinetic frictional relaxation term essentially vanishes. This leads to a significant suppression of the $E_\parallel$ "spike" in the preheat layer in the fully kinetic case.

This preheat layer electric-field spike corresponds to the "precursor" electric shock layer described by Jaffrin and Probstein [10]. For comparison, a profile based on their semianalytic shock solution is also included in Fig. 4 (top). We note that the derivation of Ref. [10] is based on a Navier-Stokes model, and thus does not correctly represent the transport for a fluid plasma model (e.g., Braginskii). In order to make a more fair quantitative comparison we have altered their solution by making the transformations $\epsilon \rightarrow \epsilon/2$ in their Eq. (3.4a) and $\epsilon \rightarrow 2\epsilon$ in their Eq. (3.5a) (which brings the ratio of electron and ion transport coefficients more into line with the estimates of Braginskii [18]). The result shows remarkably good agreement with the hybrid iFP solution in the precursor shock layer at the upstream preheat layer edge, but agrees only qualitatively elsewhere.

We include an analysis of the charge separation $\delta_E = \epsilon_0 \partial_x E_\parallel$ [13] in Fig. 4 (bottom). Given that $\lambda_D/\lambda_{ii} \ll 1$, we see that, unsurprisingly, the charge separation for this problem is quite small. We also again see the precursor shock collapse in the fully kinetic case. However, the charge separation predicted by the semianalytic solution in the preheat layer

is within an order of magnitude of that shown by the hybrid simulation. Reference [10] estimates the precursor shock thickness to be $l/\lambda_{ii}^{\mathrm{US}} \sim M/\sqrt{m_e/m_i}$ (here, $l/\lambda_{ii}^{\mathrm{US}} \sim 6$), which is about a factor of 2 smaller than the width estimated from the hybrid and fully kinetic simulations.

IV. CONCLUSIONS

We have performed converged fully kinetic simulations of strong steady-state planar plasma shocks. We have found that the differences between hybrid and fully kinetic simulations are limited to the electron preheat region of the shock and, specifically, to the electron-temperature profile therein; the differences are focused at the upstream edge, where the temperature gradient length scale is smallest and the electron-temperature Knudsen number is largest. We find the electron heat flux exhibits stiffness across various models, with only small adjustments to the heat-flux slope near the upstream edge of the preheat layer. However, while its spatial profile is qualitatively unchanged, the heat flux exhibits significant nonlocality in the fully kinetic case. Further, in other parametric regimes, such as ICF implosions with much stronger *spherically converging* shocks, or multi-ion systems, this cannot necessarily be assumed to be the case and will be a subject of future work. We find that a heat flux computed using the LMV model [20–22] using kinetic-electron moments is reasonably consistent with the kinetic-electron heat flux (including the nonlocal phase-space behavior), while the corresponding Braginskii heat flux is not, which provides a level of confidence in the capability of the LMV model to recapture the kinetic moment profiles if used in a hybrid simulation. The electric field $E_\parallel$ at the preheat layer leading edge is found to be very similar to that predicted by a semianalytic fluid solution [10], but with minimal charge separation due to the gradient smoothing effect of the kinetic electrons.

APPENDIX: NORMALIZATION

In our simulations we use the following normalizing constants for the downstream quantities:

$$n^* = 1 \times 10^{22} \text{ (cm}^{-3}), \quad T^* = 1 \times 10^4 \text{ (eV)},$$
$$q^* = 6.022 \times 10^{-19} \text{ (C)}, \quad m^* = 1.6726 \times 10^{-24} \text{ (g)}.$$

From these, the normalizing speed u^*, time τ^*, and length L^* may be defined as the ion thermal speed, inverse ion-ion

collision frequency, and ion-ion mean free path, respectively:

$$u^* = 9.787 \times 10^7 \text{ (cm s}^{-1}), \quad \tau^* = 2.085 \times 10^{-10} \text{ (s)},$$

$$L^* = 2.041 \times 10^{-2} \text{ (cm)}.$$

We estimate the Debye length in the downstream as approximately $\lambda_D^* = 7.43 \times 10^{-7}$ (cm), such that $\lambda_D^*/L^* \approx 3 \times$ 10^{-5}, firmly in the quasineutral regime. We further note that in the quasineutral limit ($\lambda_D^*/L^* \ll 1$), the *normalized* profiles of the moment quantities (temperature, etc.) through the shock will be self-similar for a given Mach number, and will not depend on the specific normalizing constants.

[1] M. J. Rosenberg, F. H. Séguin, P. A. Amendt, S. Atzeni, H. G. Rinderknecht, N. M. Hoffman, A. B. Zylstra, C. K. Li, H. Sio, M. Gatu Johnson, J. A. Frenje, R. D. Petrasso, V. Y. Glebov, C. Stoeckl, W. Seka, F. J. Marshall, J. A. Delettrez, T. C. Sangster, R. Betti, S. C. Wilks *et al.*, Phys. Plasmas **22**, 062702 (2015).

[2] M. J. Rosenberg, H. G. Rinderknecht, N. M. Hoffman, P. A. Amendt, S. Atzeni, A. B. Zylstra, C. K. Li, F. H. Séguin, H. Sio, M. G. Johnson, J. A. Frenje, R. D. Petrasso, V. Y. Glebov, C. Stoeckl, W. Seka, F. J. Marshall, J. A. Delettrez, T. C. Sangster, R. Betti, V. N. Goncharov *et al.*, Phys. Rev. Lett. **112**, 185001 (2014).

[3] H. G. Rinderknecht, H. Sio, C. K. Li, A. B. Zylstra, M. J. Rosenberg, P. Amendt, J. Delettrez, C. Bellei, J. A. Frenje, M. Gatu Johnson, F. H. Séguin, R. D. Petrasso, R. Betti, V. Y. Glebov, D. D. Meyerhofer, T. C. Sangster, C. Stoeckl, O. Landen, V. A. Smalyuk, S. Wilks *et al.*, Phys. Rev. Lett. **112**, 135001 (2014).

[4] W. T. Taitano, A. N. Simakov, L. Chacón, and B. D. Keenan, Phys. Plasmas **25**, 056310 (2018).

[5] A. N. Simakov, B. D. Keenan, W. T. Taitano, and L. Chacón, Phys. Plasmas **24**, 092702 (2017).

[6] B. D. Keenan, A. N. Simakov, L. Chacón, and W. T. Taitano, Phys. Rev. E **96**, 053203 (2017).

[7] B. D. Keenan, A. N. Simakov, W. T. Taitano, and L. Chacón, Phys. Plasmas **25**, 032103 (2018).

[8] J. D. Jukes, J. Fluid Mech. **3**, 275 (1957).

[9] V. D. Shafranov, Zh. Eksp. Teor. Fiz. **32**, 1453 (1957) [Sov. Phys. JETP **5**, 1183 (1957)].

[10] M. Y. Jaffrin and R. F. Probstein, Phys. Fluids **7**, 1658 (1964).

[11] M. S. Grewal, Phys. Fluids **16**, 561 (1973).

[12] T. O. Masser, J. G. Wohlbier, and R. B. Lowrie, Shock Waves **21**, 367 (2011).

[13] Y. B. Zel'dovich and Y. P. Raizer, in *Physics of Shock Waves and High-Temperature Hydrodynamic Phenomena*, 2nd ed., edited by W. D. Hayes and R. F. Probstein (Academic Press, Cambridge, MA, 1967), Vol. II.

[14] M. Casanova, O. Larroche, and J. P. Matte, Phys. Rev. Lett. **67**, 2143 (1991).

[15] O. Larroche, Phys. Fluids B **5**, 2816 (1993).

[16] F. Vidal, J. P. Matte, M. Casanova, and O. Larroche, Phys. Fluids B **5**, 3182 (1993).

[17] A. N. Simakov and K. Molvig, Phys. Plasmas **21**, 024503 (2014).

[18] S. I. Braginskii, in *Reviews of Plasma Physics* (Consultants Bureau, New York, 1965), Vol. 1, pp. 205–311.

[19] S. I. Braginskii, Zh. Eksp. Teor. Fiz. **33**, 459 (1957) [Sov. Phys. JETP **6**, 358 (1958)].

[20] J. F. Luciani, P. Mora, and J. Virmont, Phys. Rev. Lett. **51**, 1664 (1983).

[21] A. Bendib, J. F. Luciani, and J. P. Matte, Phys. Fluids **31**, 711 (1988).

[22] G. P. Schurtz, P. D. Nicolaï, and M. Busquet, Phys. Plasmas **7**, 4238 (2000).

[23] D. Cao, G. Moses, and J. Delettrez, Phys. Plasmas **22**, 082308 (2015).

[24] F. Vidal, J. P. Matte, M. Casanova, and O. Larroche, Phys. Plasmas **2**, 1412 (1995).

[25] J. P. Matte and J. Virmont, Phys. Rev. Lett. **49**, 1936 (1982).

[26] M. Tzoufras, A. Tableman, F. S. Tsung, W. B. Mori, and A. R. Bell, Phys. Plasmas **20**, 056303 (2013).

[27] W. S. Zhang, H. B. Cai, B. Du, D. G. Kang, S. Y. Zou, and S. P. Zhu, Phys. Rev. E **103**, 023213 (2021).

[28] J. D. Huba, *NRL Plasma Formulary Supported by The Office of Naval Research* (Naval Research Laboratory, Washington, D.C., 2013), pp. 1–71.

[29] S. E. Anderson, W. T. Taitano, L. Chacón, and A. N. Simakov, J. Comput. Phys. **419**, 109686 (2020).

[30] W. T. Taitano, L. Chacón, and A. N. Simakov, J. Comput. Phys. **365**, 173 (2018).

[31] W. T. Taitano, B. D. Keenan, L. Chacón, S. E. Anderson, H. R. Hammer, and A. N. Simakov, Comput. Phys. Commun. **263**, 107861 (2021).

[32] W. T. Taitano, L. Chacón, A. N. Simakov, and S. E. Anderson, Comput. Phys. Commun. **258**, 107547 (2021).

[33] K. J. Bowers, B. J. Albright, L. Yin, B. Bergen, and T. J. Kwan, Phys. Plasmas **15**, 055703 (2008).

[34] K. J. Bowers, B. J. Albright, B. Bergen, L. Yin, K. J. Barker, and D. J. Kerbyson, in *Proceedings of the 2008 ACM/IEEE Conference on Supercomputing* (IEEE Press, Piscataway, NJ, USA, 2008), pp. 1–11.

[35] K. J. Bowers, B. J. Albright, L. Yin, W. Daughton, V. Roytershteyn, B. Bergen, and T. Kwan, J. Phys.: Conf. Ser. **180**, 012055 (2009).

[36] E. E. Meshkov, Sov. Fluid Dyn. **4**, 101 (1969).

[37] E. S. Weibel, Phys. Rev. Lett. **2**, 83 (1959).

[38] A. Savitzky and M. J. E. Golay, Anal. Chem. **36**, 1627 (1964).

[39] A. N. Simakov and K. Molvig, Phys. Plasmas **23**, 032115 (2016).